N. Hosseini, M. Tadjfar, A. Abbà
Configuration Optimization of Two Tandem Airfoils at Low Reynolds Numbers
Applied Mathematical Modelling, Vol. 102, 2022, p. 828-846
doi:10.1016/j.apm.2021.10.029

Configuration optimization of two tandem airfoils at low Reynolds numbers

N. Hosseini [a], M. Tadjfar [a], A. Abba [b]

[a] *Aerospace Engineering Department, Turbulence and Multi-Phase Flow Laboratory, Amirkabir University of Technology, Tehran, Iran* [b] *Dipartimento di Ingegneria Aerospaziale, Politecnico di Milano, Via La Masa 34, Milano 20156, Italy*

A B S T R A C T

Optimization was used to find the best configuration of two airfoils in tandem placed into an incoming flow. Upstream airfoil (forefoil) was pitching at a fixed frequency, while the downstream airfoil (hindfoil) was kept at a fixed angle of attack. Study was performed at a low Reynolds number of 30,000 based on chord length. Selig-Donovan 7003 (SD7003) was used for both airfoils, which is a high-performance airfoil specially designed for low Reynolds number flows. The optimization studies were conducted using a genetic algorithm (GA) to maximize aerodynamic performance. The design variables in this study were: horizontal and vertical spacing between the airfoils and hindfoil's angle of attack. Since the optimization process is time-consuming, machine learning was used to train four artificial neural networks (ANNs) to be coupled with genetic algorithm to reduce the computational cost. Two separate optimization cases were considered at two different orders of magnitude in pitching amplitudes of the forefoil, while the pitching frequency was kept at constant value. We found that in both cases, optimum tandem configurations had a smaller combined drag coefficient in comparison with the addition of two separate airfoils. The case with high pitching amplitude produced higher magnitude of lift, while the low amplitude case resulted in a significant improvement in aerodynamic performance.

1. Introduction

Micro-air vehicles (MAVs) are receiving increasing attention due to their wide variety of applications. MAVs with tandem wings were inspired by dragonfly flight at low Reynolds numbers. Having a wing with two airfoils in tandem configuration have advantages over single-airfoil counterpart in terms of higher fuel efficiency and lower drag [1]. Different classifications of MAVs are: fixed-wing, flapping-wing, fixed and flapping wing configuration [2]. LaMantia and Dabnichki [3] studied the influence of airfoil shape on the aerodynamic performance of the wing. In particular, they studied the effect of thickness on pitching symmetric 4-digit NACA airfoils. MAVs fly at low Reynolds numbers and at these conditions, near-stall and post-stall flight would occur during maneuvers. Hence, the choice of an appropriate high-performance airfoil is required. We used SD7003 airfoil that was specifically designed to generated high aerodynamic performance at low Reynolds numbers. This airfoil has a very stable laminar separation bubble with standard transition and turbulent reattachment at low Reynolds numbers [4–6].

Nomenclature

f	pitching frequency
k	pitching reduced frequency [$k = 0.5$]
U_∞	free stream velocity [=3.77 m/s]
C	chord length [=0.12 m]
a	forefoil angle of attack
a_0	mean forefoil angle of attack [=8°]
α	hindfoil angle of attack
L	lift force
D	drag force
T	pitching time cycle
C_l	lift force coefficient
C_d	drag force coefficient
A	pitching motion amplitude
Re	Reynolds number based on chord length
L/D	aerodynamic performance
ω	vorticity
h	vertical spacing between two airfoils
l	horizontal spacing between two airfoils

In an experimental study conducted at low Remolds numbers, Scharpf and Mueller [7] investigated the flow over two closely-placed identical fixed-wings in a tandem configuration at different angles of attack. They found that the addition of the upstream airfoil resulted in attached flow on the downstream airfoil at high angles of attack. The changes in the flow field of tandem configuration resulted in reduction of total drag force and increasing of total lift force, culminating into a significant increase in the lift to drag ratio (L/D) defined as the aerodynamic performance. In another experimental study of low Reynolds number flows, Jones et al. [8] performed an investigation on different tandem configurations of two identical flat plates. The effect of changing the vertical and horizontal spacing between the wings and also angle of attack of the airfoils were studied. They reported that for certain tandem configurations, total lift force was increased and stall angle was delayed. They suggested that due to this improvement of post-stall flow, tandem configurations can be considered as a valid form of passive flow control.

Faure et al. [9] experimentally examined flow around a two NACA23012 airfoils placed in tandem. The hindfoil was at half the chord length of the forefoil in a T-tail type arrangement. They reported measured aerodynamic coefficients for both wing and tail at large angles of attack. They argued that the particulars of the horizontal or vertical spacing can have a great influence on the interaction of the leading-edge vortex (LEV) and trailing-edge vortex (TEV) separated from the forefoil with hindfoil. In a numerical study, Faure et al. [10] investigated the flow around two SD7003 airfoils in tandem arrangement. They performed a parametric study of different horizontal and vertical spacing between the two airfoils. They reported a maximum gain in lift coefficient was achieved with zero horizontal spacing and a negative vertical spacing between the airfoils for angles of attack between 15° and 35°.

Rival et al. [11] in a series of experiments investigated a pitching or plunging forefoil and its interaction with a fixed hindfoil. The angle of attack of the hindfoil and vertical spacing between the two airfoils were changed during the experiments. They reported that the combined time-averaged lift force for the tandem airfoils did not alter significantly. However, combined time-averaged drag force was reduced in some configurations. Lee [12] examined the effect of phase difference between two pitching NACA0012 airfoils placed in tandem. The airfoils were pitching sinusoidally with the same frequency and mean angle of attack at two different phases. The results showed that the axial spacing and phase difference influenced the formation of LEV on the hindfoil. The absence of LEV-induced transient effects significantly altered the force balance on the hindfoil. Lua et al. [13] derived an approximate mathematical model for the influence of horizontal spacing and phase difference for two pitching and plunging identical airfoils. They found that increasing horizontal spacing and decreasing phase difference between the tandem airfoils have a similar effect on the aerodynamic performance of the downstream airfoil.

These studies, experimental or numerical, were a parametric study on the effect of geometrical spacing, angle of attack or phase difference between two tandem airfoils on their overall aerodynamic performance. Here, we used an optimization process to find the optimum configuration for two SD7003 airfoils in tandem. Different methods have been developed for optimization process, classical and heuristic methods. Classical methods are gradient based and are applicable in continuous domain. Heuristic methods are applicable in both continuous and dispersed domains.

Kamari et al. [4] and Tadjfar and Kamari [5] used genetic algorithms to perform an optimization study on separation control of an SD7003 airfoil at a low Reynolds number. They optimized several design parameters related to active flow control to maximize lift-to-drag ratio of the airfoil. During the optimization process, the solver has to be called many times and this process can be very computationally intensive. One way to reduce this computational cost is by coupling the genetic

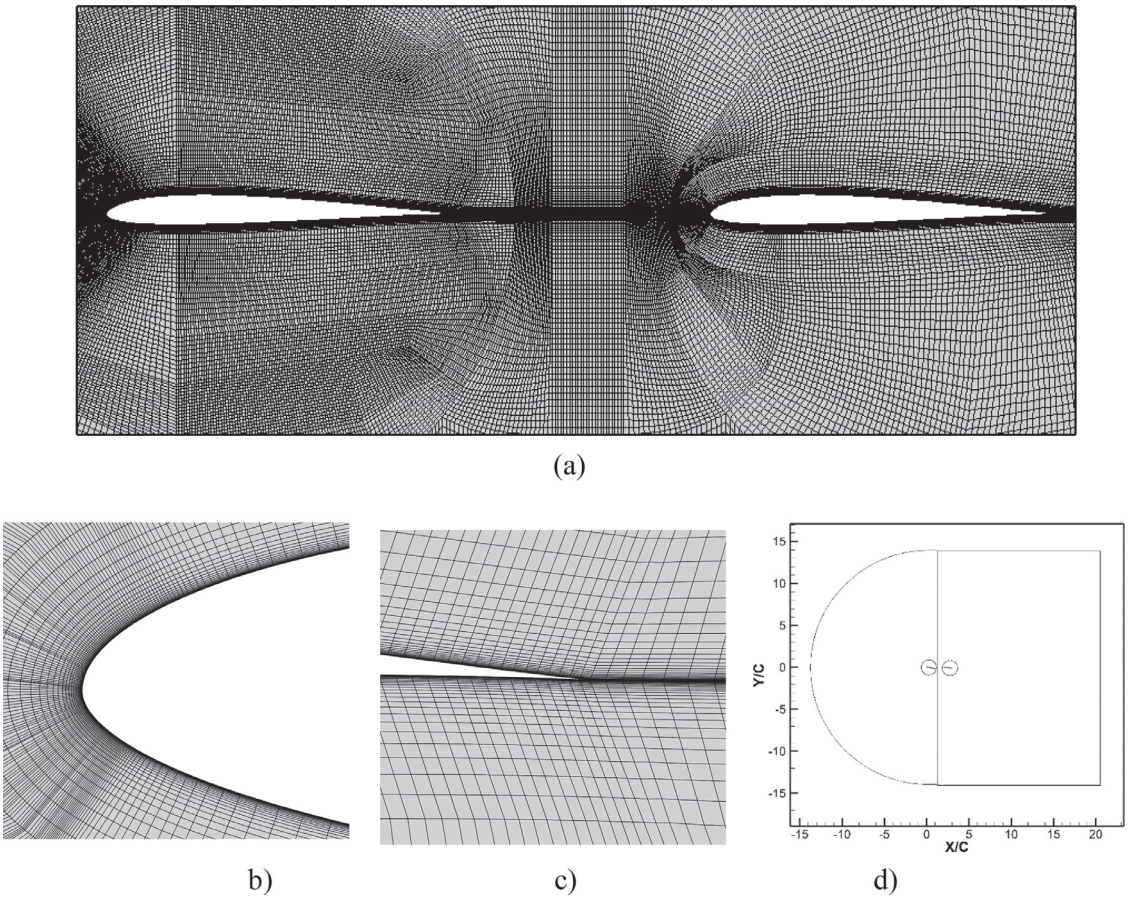

Fig. 1. (a) Structured grid, (b) near leading edge, (c) near trailing edge, and (d) computational domain.

algorithm with trained artificial neural networks [4,5] to estimate the aerodynamic parameters. In a recent study, Balla et al. [14] proposed a novel neural network for the prediction the pressure at a number of selected points on the aerodynamic shape instead of predicting the aerodynamic coefficients directly.

In the present study, the effect of placing a stationary hindfoil downstream of an identical pitching forefoil in tandem configuration was investigated at low Reynolds number of 30,000 based on the chord length. Following the authors previous works [4,5], SD7003 was chosen as a high-performance airfoil at these low Reynolds numbers. Two optimization studies at two different pitch amplitudes of the forefoil were conducted to find optimum design configuration with maximum aerodynamic performance. Aerodynamic performance is defined as the combined total time-averaged value of lift-to-drag ratio of both airfoils. Three design variables were considered in this study: horizontal and vertical spacing between the airfoils, and the angle of attack of the hindfoil. A genetic algorithm was coupled with four artificial neural networks (ANNs) to perform the optimization process. This coupling reduced the overall computational cost.

2. Simulation set-up

2.1. Geometry and mesh

An asymmetric Selig-Donovan 7003 (SD7003) airfoil was selected for both airfoils with 0.09C maximum thickness. This airfoil has high aerodynamic performance at the low (transitional) Reynolds number of this study. Computational domain and grid clustering in the vicinity of leading edge and trailing edge are shown in Fig. 1. The domain was extended approximately 14 chord lengths into the upstream direction of the airfoil and 18 chords into the downstream. To allow for pitching motion, a circular structured-grid around the forefoil was implemented to separate moving and stationary zones. By moving of forefoil with a prescribed motion, the grid inside the circular zone moved with the airfoil like a rigid-body motion without grid deformation. Another circular zone was also implemented around the hindfoil for smooth changing of the angle of attack during the optimization process. The centers of these circular zones corresponded to quarter chord point of the forefoil and three quarters chord point on the hindfoil. Horizontal and vertical spacing between the airfoils was adjusted the center of the second circular zone inside the rectangular zone shown in Fig. 1(a). A structured C-type grid was generated

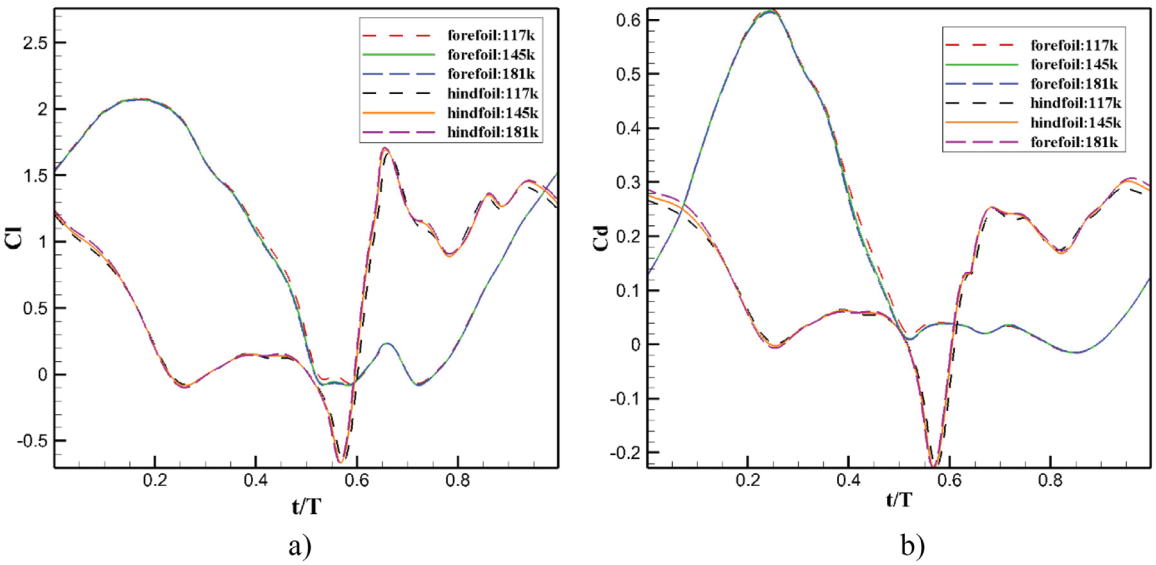

Fig. 2. Influence of grid size on (a) lift coefficient and (b) drag coefficient for forefoil and hindfoil.

and the grid density was high around the leading edge of the forefoil and close to all airfoil walls. The boundary layers formed near the airfoil walls were fully resolved and y^+ values were below 1.0 at all the nodes adjacent to the airfoil's surfaces. The skewness value was below 0.38 within the circular zones. All the mesh regenerations during the optimization process were performed automatically within the framework described above.

2.2. Flow solver

The two-dimensional unsteady Reynolds averaged Navier-Stokes equations were solved using a finite-volume solver. we used k-ω SST with local correlation-based transition model developed by Menter et al. [15,16]. This model was found successful in predicting the separation bubble and transition accurately on this airfoil at low Reynolds number [4,5]. The numerical simulations were performed using second-order spatial and first-order temporal discretization. Pressure-velocity coupling with SIMPLE algorithm was implemented. The following boundary conditions were applied: constant velocity at the inlet, zero gradient with a constant pressure at the outlet and no slip condition along the airfoil's surfaces. Both OpenFOAM and Ansys Fluent were used for solution and valdation purposes.

2.3. Grid size and time-step

Independence of the numerical simulations from the choice of grid size and time-step size were established. Three grids of different mesh sizes were considered. The distributions of lift and drag coefficients over one-time cycle for both airfoils are compared for all three grids. The three grids composed of 117,000, 145,000, and 181,000 cells, respectively. The comparisons for tandem configuration with minimum horizontal spacing between the two airfoils are presented in Fig. 2. As shown, for the grid with 145,000 cells, we had reached grid-independent results and this grid was chosen as the minimum grid size in this optimization study. During the optimization process, as the horizontal spacing between the airfoils was increased an array of cells of equal size were added to the grid to cover the extra distance in between the airfoils.

Time-step size independence study was also performed for three different time-step sizes. The distribution of lift and drag coefficients of two tandem airfoils for three different time-step sizes during one time-cycle are presented in Fig. 3. Based on these results, the time-step size of 0.0001 s was found sufficient and chosen for all simulations. This time-step size was in the order of time-step size recommended by Tadjfar and Asgari [17,18] to study unsteady flow of a pitching airfoil. They found that the time-step size of $\Delta t = t^*/230$ where $t^* = \min(\frac{c}{U_\infty}, \frac{1}{f})$ was required to simulate unsteady pitching-airfoil flows accurately, where f represented the pitching frequency, C was the airfoil chord length and U_∞ was the free-stream velocity.

3. Validation

3.1. Stationary tandem airfoils

To show that the solver used was capable of capturing the required flow in our optimization study accurately, one has to validate it against similar available experimental and numerical reported data. To validate our numerical simulations,

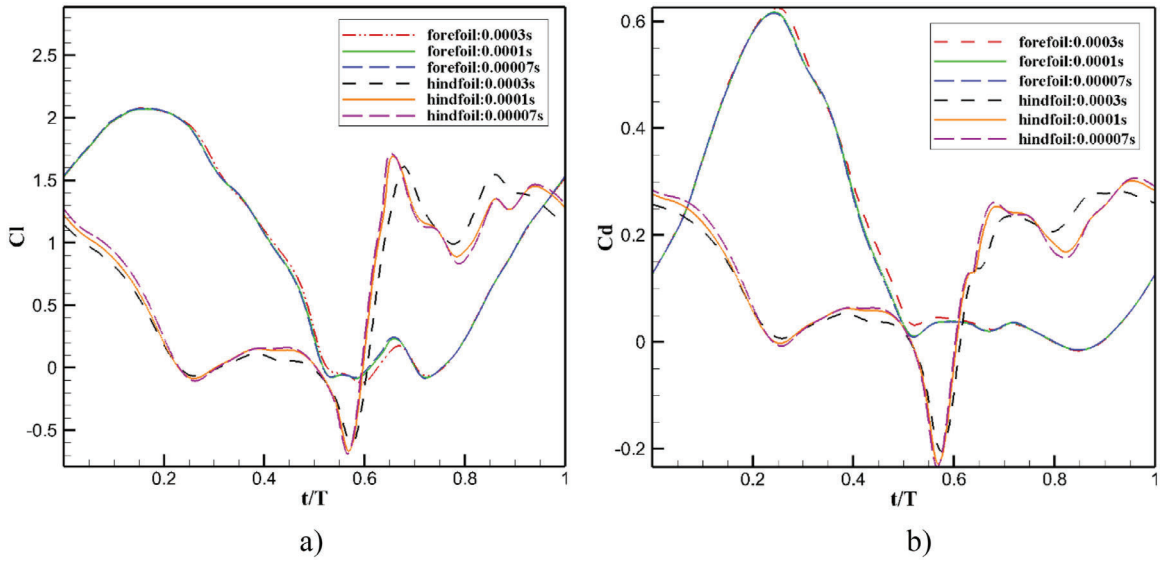

Fig. 3. Influence of time step size on (a) lift coefficient and (b) drag coefficient for forefoil and hindfoil.

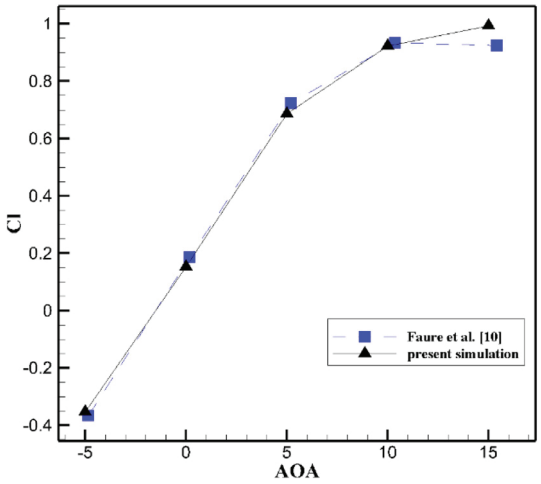

Fig. 4. Comparison of mean lift coefficient of two SD7003 airfoils in tandem at $R = 100{,}000$ between our simulations and simulations of Faure et al. [10].

we calculated the mean lift coefficients for two SD7003 airfoils in stationary tandem configuration at Reynolds number of 100,000. In this configuration, the angle of attack of both airfoils are the same with horizontal and vertical spacing of 0.5C and 0C, respectively. Results of our simulations are compared to numerical data of Faure et al. [10]. This comparison is presented in Fig. 4, where there is a good agreement between the two simulation results.

3.2. Pitching single airfoil

Here, we simulated the flow over a single pitching SD7003 airfoil at the Reynolds number of 30,000. We have compared the results of our simulations with available experimental data: lift coefficients from PIV and direct force measurements of Rival et al. [11] and "*equivalent pure-plunge motion*" of Ol et al. [19]. The comparisons of lift coefficient are presented in Fig. 5. There was a maximum phase advance of 0.04t/T in the effective angle of attack distribution for the pure-pitch motion as stated in [20], so the direct force data for pitching motion is shifted by 0.04t/T.

Here, the airfoil had a sinusoidal pitching motion about its quarter-chord point:(see Fig. 8)

$$a = a_0 + A\ sin(2\pi ft) \tag{1}$$

where a_0 and A represent mean angle of attack and amplitude of oscillating motion, respectively. The value of mean angle of attack was 8° and the amplitude of the oscillating motion was 14.1°. Reduced frequency of pitching motion is defined as:

$$k = \frac{\pi fC}{U_\infty} \tag{2}$$

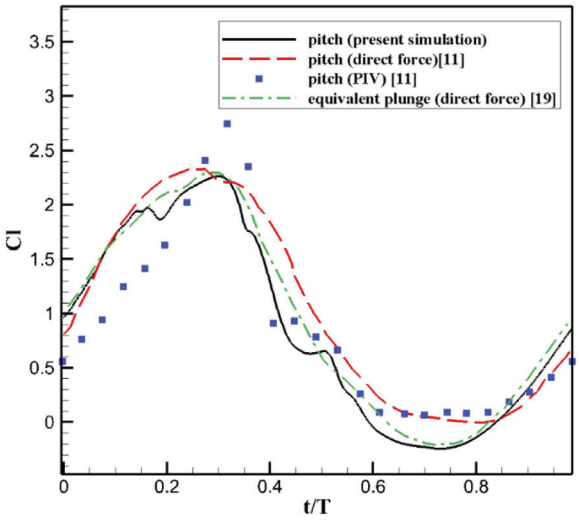

Fig. 5. Comparison of lift coefficient of a single pitching SD7003 airfoil at $Re = 30{,}000$ with experiments of [11,19].

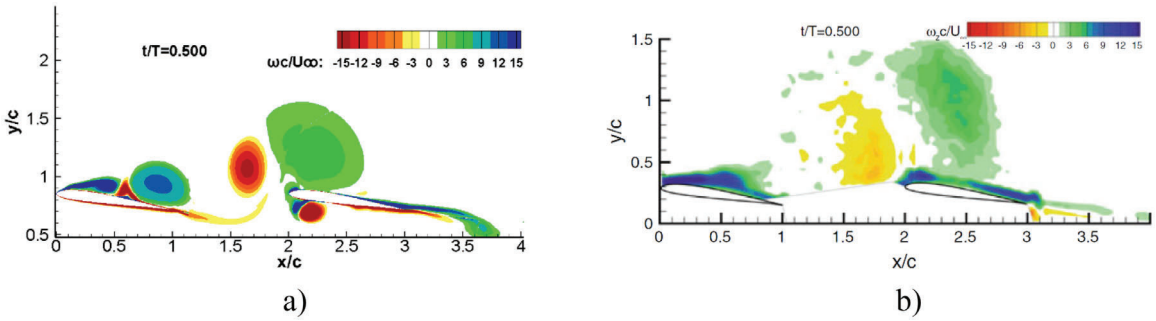

Fig. 6. Comparison of non-dimensional vorticity field at mid period (a) present simulation (b) experimental data of [11].

where f represents the pitching frequency, C the airfoil chord length and U_∞ the free-stream velocity. The reduced frequency of pitching motion used in the experiments by Rival et al. [11] and Ol et al. [19] was $k = 0.25$. As shown in Fig. 5, there was a relatively good agreement between our results and the direct force measurements. We also had the same discrepancy as in the experiments with PIV estimations.

3.3. Pitching forefoil with fixed hindfoil

The vortex interactions of a tandem configuration placed in an incoming flow at $Re = 30{,}000$ of a pitching SD7003 forefoil with a stationary SD7003 hindfoil was compared to PIV data of Rival et al. [11]. Comparison of vorticity contours at mid oscillation cycle ($t/T = 0.5$) is presented in Fig. 6. In these experiments, the forefoil oscillated with an equivalent pure-plunge motion. The hindfoil was fixed at 8° angle of attack and was positioned one chord away from the trailing edge of the forefoil. In the experimental setup, there was a shadow zone on the pressure side of the airfoils (bottom surface), hence there was no velocity measurements there. As shown in Fig. 6, measured vorticity contours on the top surfaces of the airfoils are in good agreement with our simulated results. Rival and Tropea [20] reported that for $k > 0.2$ a single LEV was shed into the wake. The LEV shed from the forefoil in our simulations was tracked and its core trajectory and convective velocity are compared to experimental measurements in Fig. 7.

4. Optimization

4.1. Problem definition

The purpose of this study was to find the optimum configuration of placing two SD7003 airfoils in tandem configuration into an incoming flow at low Reynolds number of 30,000. The forefoil was pitching at a constant frequency of 5 Hz ($k = 0.5$) in accordance to Eq. (1) and the hindfoil was kept at a fixed angle of attack. This reduced frequency was in the order of forward flight reduced frequency for most birds, bats, and large insects ($0.05 < k < 0.3$) [20] which are an inspiration for MAVs at low Reynolds numbers. The forefoil oscillated in a sinusoidal motion around a non-zero mean angle of attack of

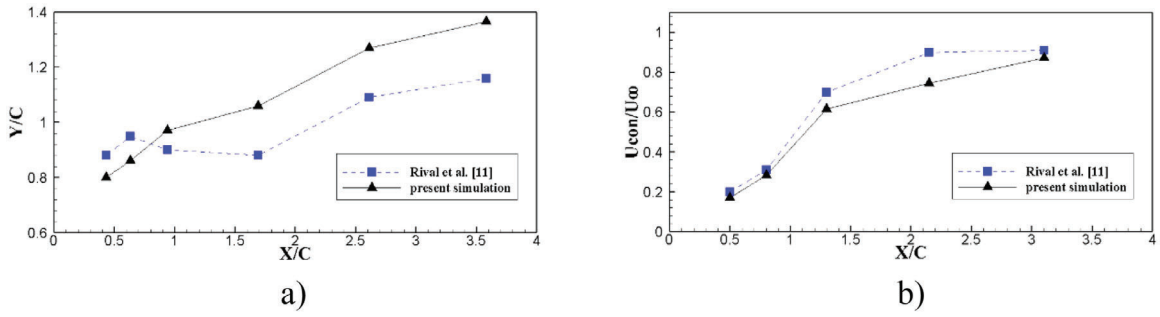

Fig. 7. Comparison between present simulation and experimental results of [11] for (a) LEV trajectory and (b) LEV convective velocity.

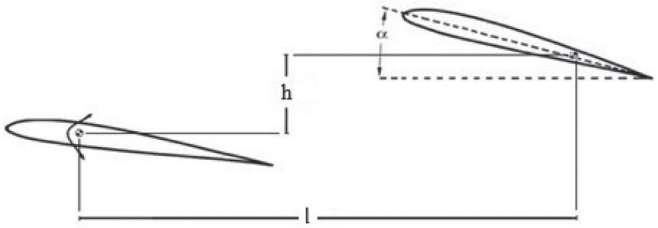

Fig. 8. Design variables investigated for optimization studies.

Table 1
Design variables bound for optimization studies.

Design variables	Range
Horizontal spacing	2C–4.5C
Vertical spacing	-0.6C–0.6C
Hindfoil angle of attack	0°–13°

$a_0 = 8°$. The level of stall and resulting shed vortices from a pitching airfoil depends on the angle of attack of the pitching motion. Hence, different vortex-airfoil interactions occur at different pitching amplitudes. Here, the amplitude of pitching motion was set at two different values of $A = 14.1°$ and $= 1°$. These values represented two different vortex-interactions with the hindfoil. These amplitudes hereafter referred to as Case 1 and Case 2, respectively.

For the optimization study, three different design variables related to the positioning of the stationary hindfoil downstream of the pitching forefoil were allowed to change. The design variables in this study were: horizontal and vertical spacing between the airfoils and hindfoil's angle of attack. These spacings were defined between the quarter-chord point of the forefoil and three quarter-chord point of the hindfoil. These parameters are illustrated Fig. 8. Based on previous studies reviewed earlier, these parameters have a great influence on the level of interaction between the wake of forefoil and the downstream hindfoil. The bounds of design variables were the same for two cases with different pitching amplitude and are presented in Table 1. The upper bound of angle of attack for hindfoil (13°) was larger than the angle of attack where static stall occurs. In the simulations all other parameters were unchanged.

4.2. Objective function

The objective function was defined as the total aerodynamic performance for both of the airfoils combined:

$$O.F. = \left(\frac{L}{D}\right)_{total} = \left(\frac{Cl_f + Cl_h}{Cd_f + Cd_h}\right) \tag{3}$$

Where Cl_f, Cd_f, Cl_h and Cd_h represent time-averaged values of lift and drag coefficients for the forefoil and hindfoil over one pitching time-cycle, respectively.

4.3. Machine learning and artificial neural networks

Optimization process is time-consuming; machine learning was used to train four artificial neural networks (ANNs) to reduce the computational cost. The trained ANNs reproduced the desired answers without having to solve the Navier-Stokes equations with CFD. A neural network can be defined as a model of reasoning based on human brain. An artificial neural

Table 2
Artificial neural networks properties.

Criteria	Value/function	Criteria	Value/function
No. of hidden layers	3 for forefoil 4 for hindfoil	Transfer function Output function	Log-sigmoid Linear function
No. of neurons	5	Data division	Random
Feeding method	Feed forward	Training function	Levenberg-Marquardt

Table 3
Genetic algorithm properties.

Criteria	Value/function	Criteria	Value/function
Population size	200	Mutation	Adaptive feasible
Crossover Method	Two points	Fitness scaling	Rank
Crossover fraction	0.8	Reproduction elite count	5% of population
Migration	Forward	Selection	Stochastic uniform

network consists of a number of very simple processors, also called neurons, which are analogous to the biological neurons in the brain. The neurons are connected by weighted links passing signals from one neuron to another. The input signals are propagated in a forward direction on a layer-by-layer basis. The network consists of an input layer of source neurons, at least one middle or hidden layer of computational neurons, and an output layer of computational neurons. The network computes its output pattern, and if there is an error (or in other words a difference between actual and desired output patterns) the weights are adjusted to reduce this error. Implementation of ANN would reduce the computational cost, since using CFD simulation for every step of the optimization process would be too expensive. Required for the objective function defined earlier, four ANNs for predicting the values of Cl_f, Cd_f, Cl_h and Cd_h were needed to be trained. An initial database of CFD was used for training the networks. The trained ANNs for Cl_f and Cd_f consisted of three hidden layers with five neurons for each layer and the trained ANNs for Cl_h and Cd_h consisted of four hidden layers with five neurons for each layer. The trained networks were feed forward type with Levenberg-Marquardt training function. Log-Sigmoid function showed a good performance as the neuron transfer function. For all networks, 70% of data was allocated to train the network, 15% to validate and 15% to test the network. The validation subset was used to check the quality of the trained ANNs, the mean squared errors between the validation data and their estimation by ANNs were monitored during the training process. In the initial phase of training, the validation errors decreased but eventually the error improvements flattened out or slightly degraded. This flattening or degradation of improvement in error had to be persistent for at least six iterations before termination decision was made. The testing subsets were not used during the training process; they were simply used as an independent check of the process. The parameters of ANNs used in this study are summarized in Table 2. It should be noted that all the results presented here are CFD solutions. All the final choices found by the GA were again reevaluated using the CFD solver and the ANNs were just used in intermediate steps and loops inside the GA algorithm.

5. Genetic algorithm

After training the ANNs, the genetic algorithm (GA) was used to find the configuration that maximized the objective function (to be more precise, minimum negative of objective function). Genetic algorithms are a family of computational models inspired by evolution. An implementation of a genetic algorithm begins with creating a population of parents. One then evaluates these structures in such a way that those parents which represent a better solution to the target problem are given more chances for generating new children. Execution of the genetic algorithm starts with an existing population. Selection is then applied to the current population to create an intermediate population. Then recombination and mutation are applied to the intermediate population to create the next population. The process of going from current population to the next population constitutes one generation in the execution of a genetic algorithm. After the process of selection, recombination and mutation is complete, the next population can be evaluated. In our optimization studies the children were created using a two-point crossover method with a fraction of 0.8. The mutation with adaptive feasible was also used to generate a child with no exact similarity to his parents. This helped to jump towards the optimum point or jump out of a local optimum point. For every optimization step we used a fixed population size of 200, but we did not use a fixed number of generations. Optimization was stopped at any generation after 50 if the average change in the objective function was is less than 10^{-6}. A rank type of fitness scaling was used for optimizations. The reproduction elite count was set to 5% of population size and a stochastic uniform method was used for selection function which selected new parents. The genetic algorithm properties are summarized in Table 3.

The optimum point found by this level of GA would actually be reevaluated using our CFD solver. The optimization process would stop, if the convergence criteria was satisfied, otherwise the newly acquired simulated case would be added to the database for training the next generation of ANNs. This process continued until the convergence criteria was met. The optimization algorithm is presented in Fig. 9.

Table 4
Optimum values of design variables for pitching amplitude of 14.1° and 1°.

	Single optimum value (Case 1)	Range of optimum values (case 1)	Single optimum value (Case 2)	Range of optimum values (Case 2)
Horizontal spacing (l /C)	2.620	2.1–4.5	4.453	4.3–4.5
Vertical spacing (h/C)	0.440	0.306–0.6	-0.135	(-0.245)–(-0.103)
Hindfoil angle of attack (α)	7.216	6–8.7	7.134	6.3–7.73
Cl_f	1.0058	0.9677– 1.0442	0.7943	0.8042–0.8092
Cd_f	0.2115	0.2050– 0.2174	0.0782	0.0786–0.0797
Cl_h	0.5850	0.4509– 0.7258	0.6305	0.5648–0.6763
Cd_h	0.0211	0.0075– 0.0483	0.0403	0.0373–0.0451
L/D_{total}	6.8407	6.6260– 6.8407	12.0277	11.7455–12.0277

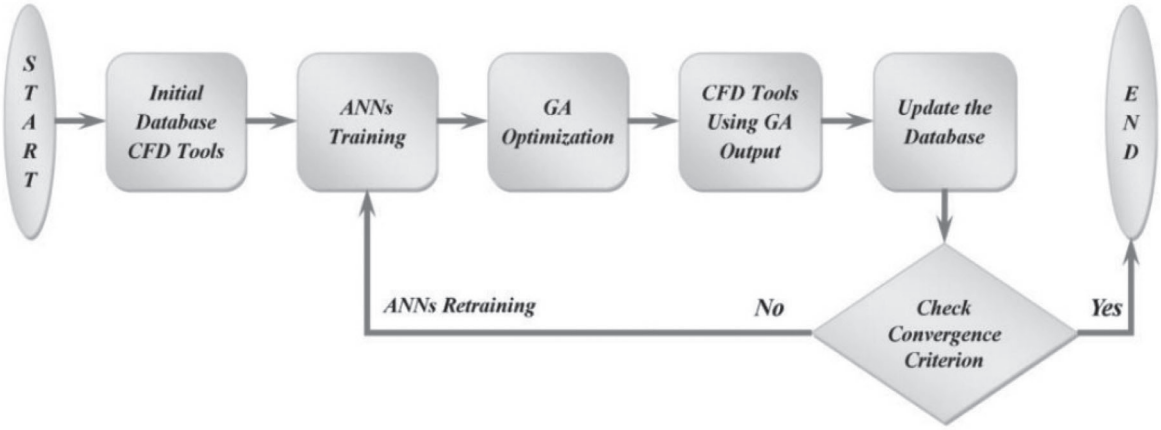

Fig. 9. Optimization algorithm.

6. Results and discussion

6.1. Two optimization cases

Two separate optimization cases were considered. The two optimization cases were at two different pitching amplitudes of the upstream forefoil: $A = 14.1°$, where the forefoil went into deep stall and $A = 1°$ where the forefoil never stalled. The final optimum configurations and their corresponding time-averaged aerodynamic coefficients and total aerodynamic performance are tabulated in Table 4. The results of optimization for both cases are presented in two columns: a single optimum value, and a range of optimum values in the table. This was due to the fact that the optimum values were chosen as the "highest value" in a range of close values with high performance rather than a distinct single value. The single value represents the case with the highest aerodynamic performance (objective function) among the range of values.

The optimum value for hindfoil angle of attack occurred in a similar range for both cases at an angle of attack of approximately 7°. The converged values of vertical spacing for Case 1 ($A = 14.1°$) occurred at a range of positive values implying that the hindfoil should be placed above the upstream forefoil. For Case 2 the opposite happened and a negative range of converged vertical spacing values were found. For horizontal spacing, the optimum position was found near the maximum possible value of the range for Case 2, however for Case 1 the data was scattered and no preferred value could be designated. Actual values from optimization steps are presented in Fig. 10 for Case 1 and in Fig. 11 for Case 2. The aerodynamic performance values versus design parameters for all CFD results: including the initial simulations required for training of ANNs and reevaluation of all the optimum points found by GA in every step of optimization are presented in those figures. A total number of 116 CFD simulations and 127 CFD simulations were performed for Case 1 and Case 2, respectively.

6.1.1. Case 1: pitching amplitude A = 14.1°

Here, optimum configuration for Case 1 with high pitching amplitude of $A = 14.1°$ is discussed and later the results of a parametric study are presented to better understand the effect of the three design variables. Vorticity contours for optimum configuration at different times during one pitching time-cycle is presented in Fig. 12. All the pitching time-cycle data presented in this paper were taken after the transient effects were convected out of the domain and the repeatability of data was stablished. Corresponding pressure distributions over the top surface of forefoil are shown in Fig. 13. In all figures, $t/T = 0$ corresponds to time in the middle of forefoil upstroke at $a_0 = 8°$ (see Eq. (1)).

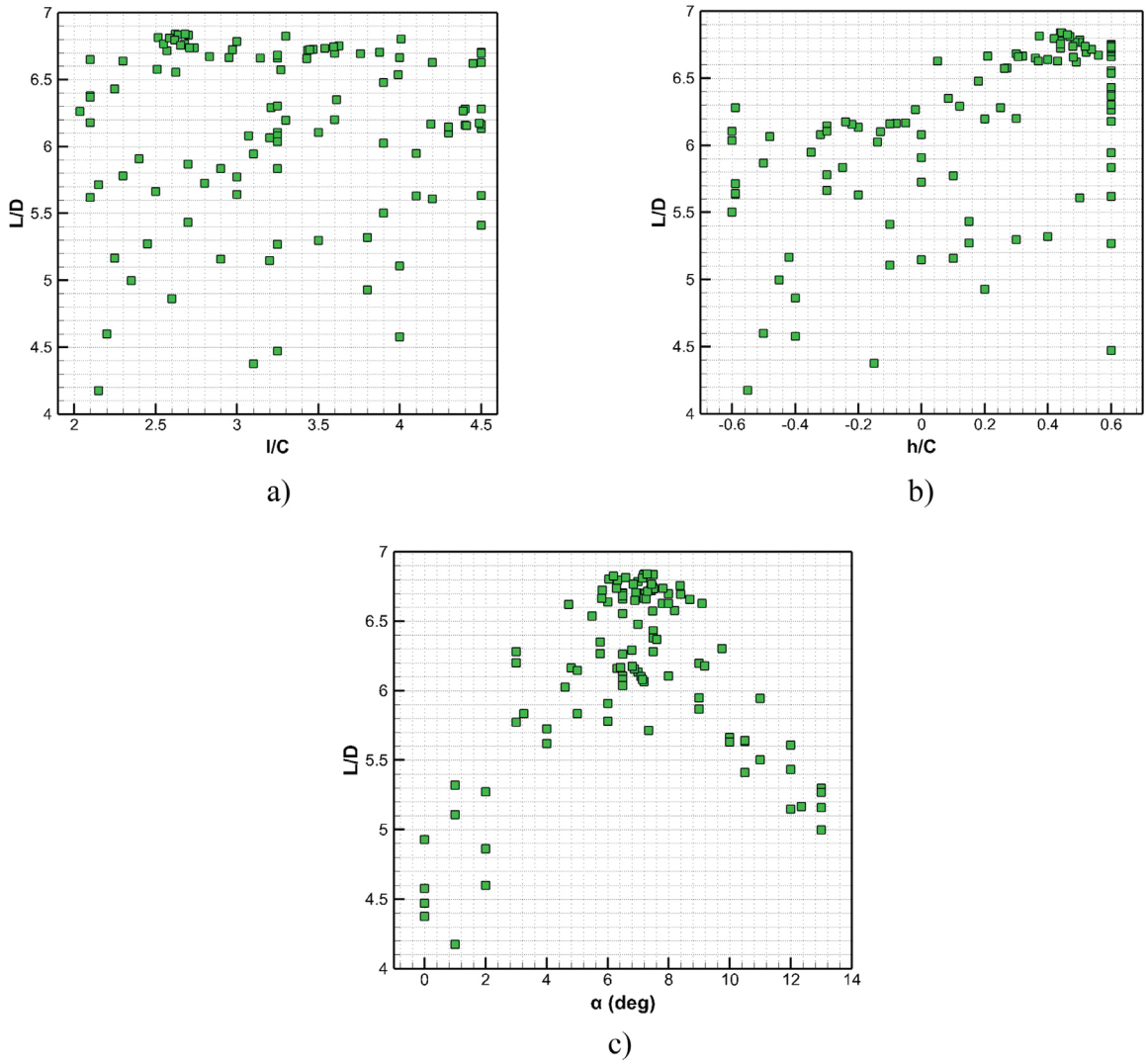

Fig. 10. Total aerodynamic performance versus (a) horizontal spacing, (b) vertical spacing, and (c) hindfoil angle of attack for Case 1.

Multiple vortices, as is characteristic of airfoils that go into deep stall, were produced over the top surface of forefoil during the pitching cycle. Initially, a small clockwise (CW) vortex was formed followed by another larger CW vortex called the main leading-edge vortex (LEV). At $t/T = 0.125$, LEV was located near the leading edge and the smaller CW was already positioned past the quarter-chord point as shown in Fig. 12(b). Both vortices grew in strength and moved downstream over the top surface of forefoil. The smaller CW vortex was near the trailing edge at $t/T = 0.375$. As the first (smaller) CW vortex reached the trailing edge, a counter clockwise (CCW) vortex was formed, this first CCW vortex interacted with the small CW vortex and this interaction resulted in weakening of both vortices as shown in Fig. 12(e). The location and movement of LEV on the top surface of forefoil can also be tracked in time by following the peaks of pressure coefficients presented in Fig. 13. When the stronger LEV reached the trailing edge a stronger CCW vortex was initiated at the trailing edge and this stronger trailing-edge vortex (TEV) was convected towards the leading edge of the hindfoil (see Fig. 12(f) and (g)). As shown in Fig 13, at $t/T = 0.75$ the entire top surface of the forefoil was at constant pressure indicating that flow separation covered the entire suction surface of the forefoil. As the angle of attack was increased in upstroke motion, pressure was increased and the flow was reattached over the top surface, and eventually lift force was also increased.

The objective function was defined by the ratio of combined lift to drag ratio of both airfoils. Variations of lift and drag forces with time over one pitching time-cycle for each airfoil separately are presented in Fig. 14. The peak of lift coefficient occurred just before maximum angle of attack ($t/T = 0.25$) as shown in Fig. 14(a). As forefoil was pitching upwards, the flow streamlines were bent in such a way that hindfoil had a lower effective angle of attack resulting in the reduction of lift and drag (with a phase delay) as shown in Fig. 14(b). At time $t/T = 0.7$, as LEV got close to the leading edge of the hindfoil lift and drag had dropped rapidly resulting in a net large negative drag (thrust) on the hindfoil. Close to ($t/T = 0.75$), as LEV

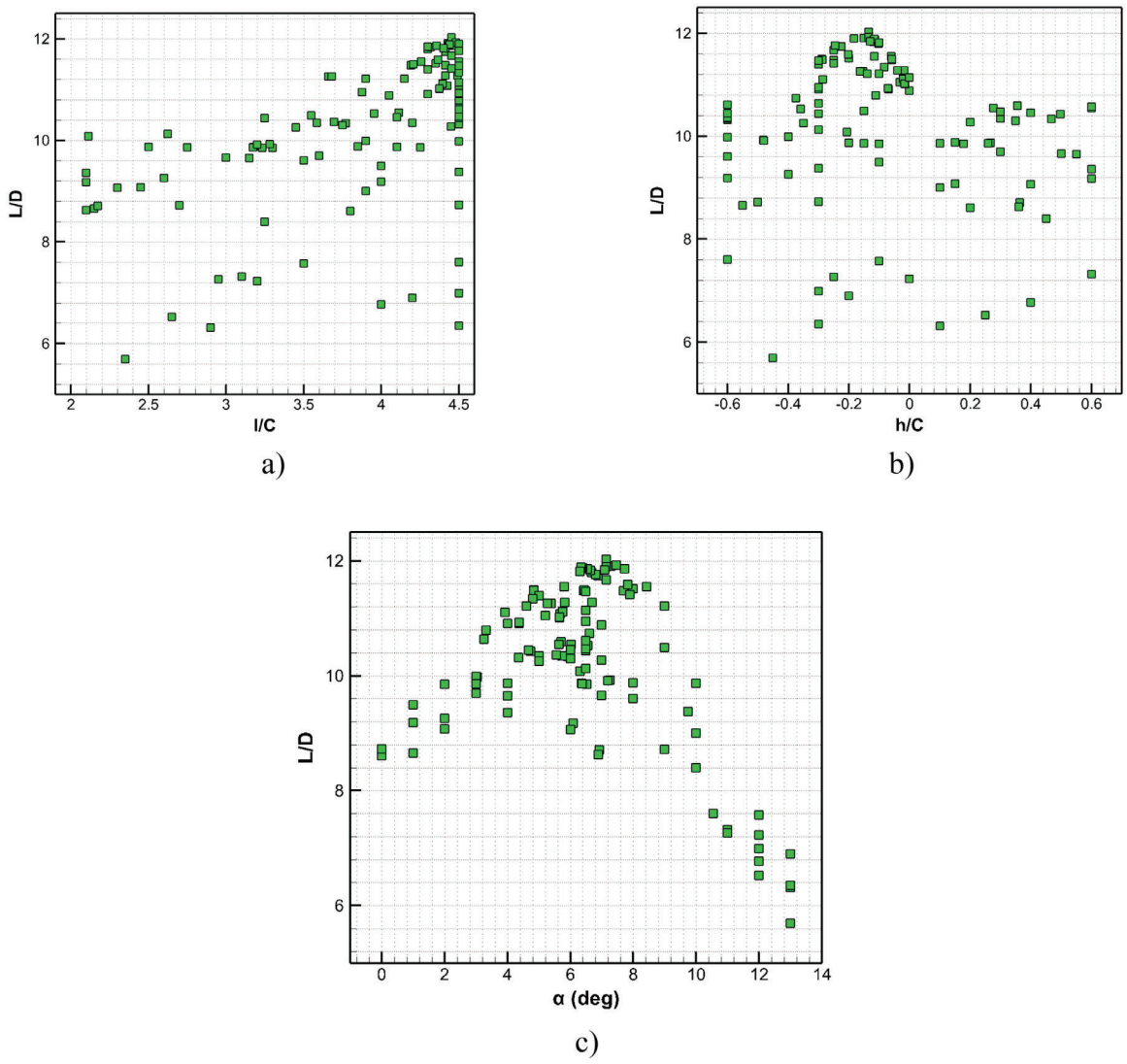

Fig. 11. Total aerodynamic performance versus (a) horizontal spacing, (b) vertical spacing, and (c) hindfoil angle of attack for Case 2.

Table 5
Parameters and results for different vertical spacings in Case 1.

Case	(l/C)	α_{hindfoil} (deg)	A (deg)	(h/C)	Cl_f	Cl_h	Cd_f	Cd_h	Cl_f+Cl_h	Cd_f+Cd_h	L/D_{tot}
case A	**2.62**	**7.216**	**14.1**	**0.44**	**1.0058**	**0.5850**	**0.2115**	**0.0210**	**1.5907**	**0.2325**	**6.84**
case B	2.62	7.216	14.1	0.2	1.0062	0.4649	0.2134	0.0148	1.4710	0.2282	6.45
case C	2.62	7.216	14.1	-0.2	1.0364	0.4553	0.2187	0.0336	1.4917	0.2523	5.91

collided with the leading edge of hindfoil, we noticed a quick reversal in lift from minimum to maximum value in a very short period of time (see Fig. 14(b)). Consequently, LEV was broken into two pieces and the core (larger piece) went under and the smaller piece went over the hindfoil. This was the perfect timing of the collision that was observed in the optimum physical configuration, as mentioned before.

6.1.2. Case 1: influence of vertical spacing

The effect of vertical spacing, h, on the trajectory of LEV was investigated. All the parameters of Case 1 were kept unchanged but the vertical spacing was allowed to change. The cases in this parametric study with their results are tabulated in Table 5.

Case A is the same as the optimal configuration of Case 1 with h/C = 0.44, and in cases B and C the vertical spacing was changed to h/C = 0.2 and h/C = -0.2, respectively. The contours of vorticity at time $t/T = 0.75$ when LEV was in the vicinity

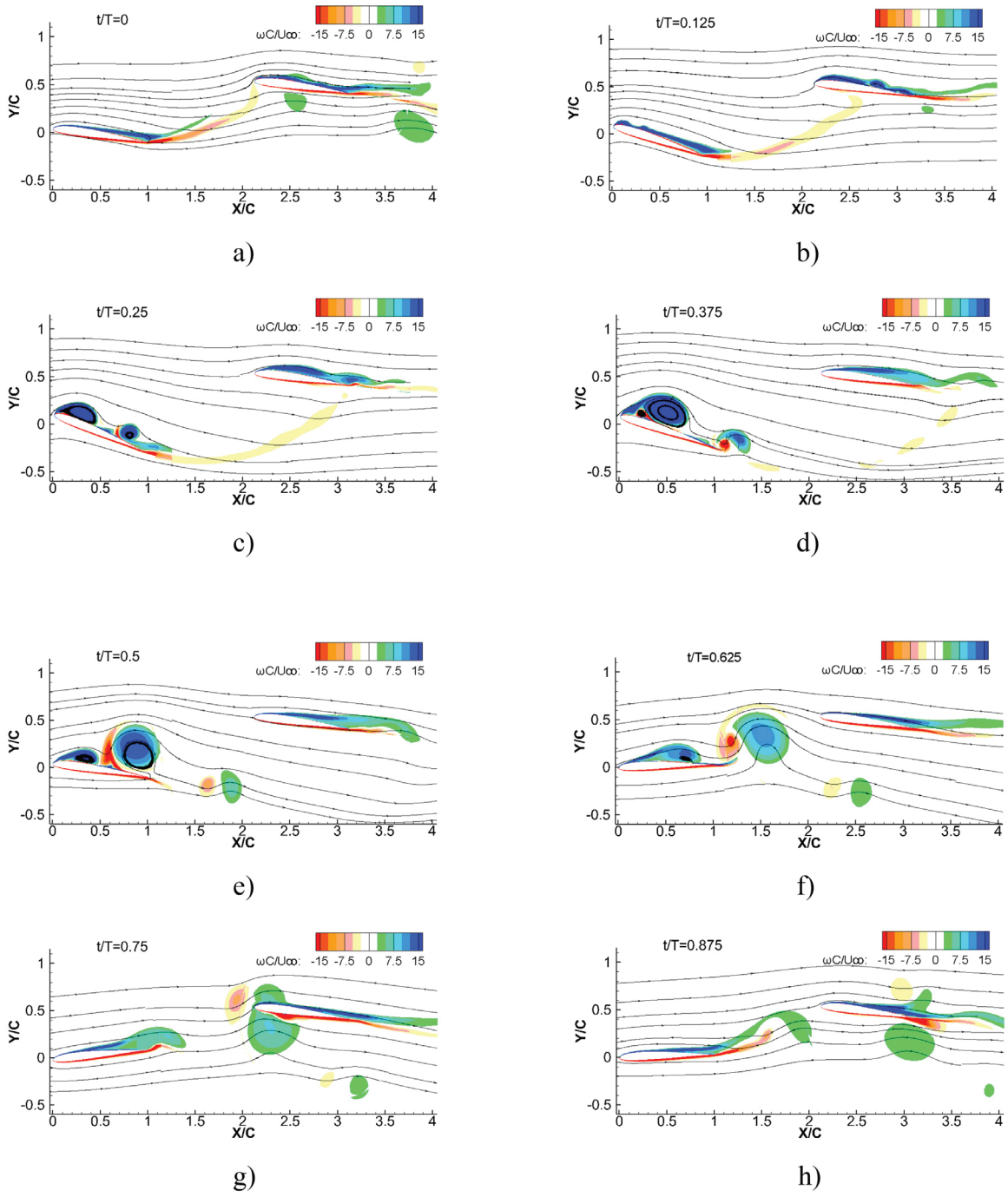

Fig. 12. Contours of non-dimensional vorticity for the optimum point of Case 1 at different times during one pitching time-cycle.

of hindfoil's leading edge for cases B and C are presented in Fig. 15. The contours in this figure should be compared with those of Fig. 12g of case A. Clearly, the perfect timing and positioning of LEV colliding with the leading edge of the forefoil did not occur for cases B and C. In case B, the forefoil was moved lower so that the larger portion of LEV after splitting into two went over the forefoil instead of below it as in Fig. 12g, and in case C the hindfoil was so low that LEV missed the hindfoil completely.

Comparison of evolution of lift and drag coefficients during one pitching time-cycle for cases A–C on the hindfoil are presented in Fig. 16. By moving hindfoil lower as in case B, lift values were generally reduced when compared to the optimal configuration (case A). The maximum value of lift that occurred after LEV collided with the hindfoil was also significantly

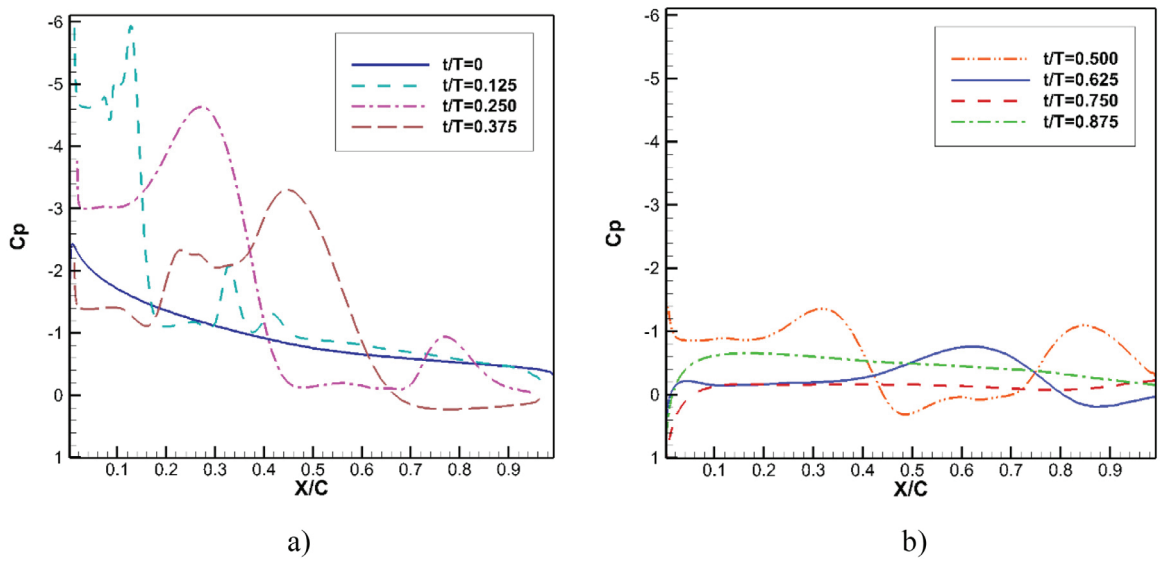

Fig. 13. Pressure coefficient distribution on the top surface of forefoil (optimum point of Case 1) over one pitching time cycle, (a) early time-cycle and (b) late time-cycle.

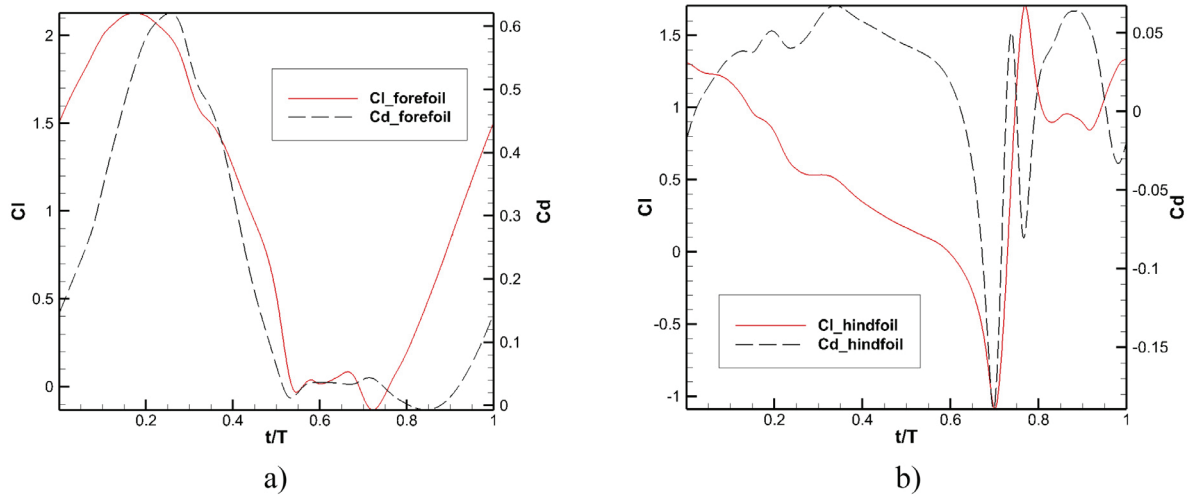

Fig. 14. Time-resolved lift and drag coefficient of (a) forefoil and (b) hindfoil (optimum point of Case 1).

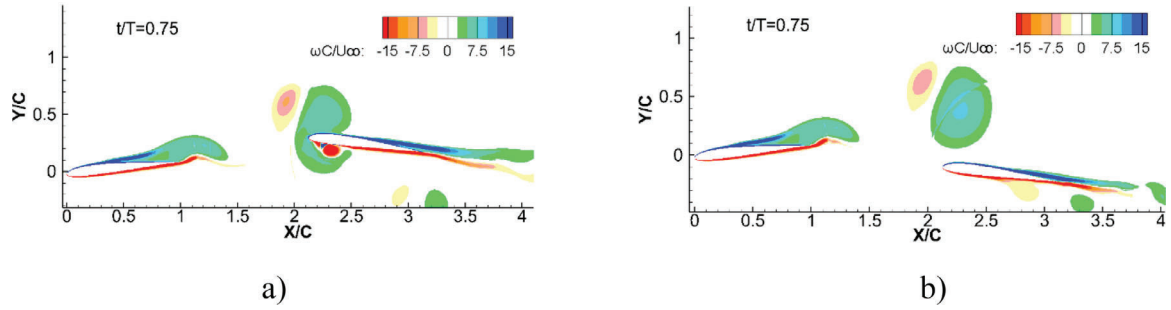

Fig. 15. Contours of non-dimensional vorticity for (a) case B, (b) case C.

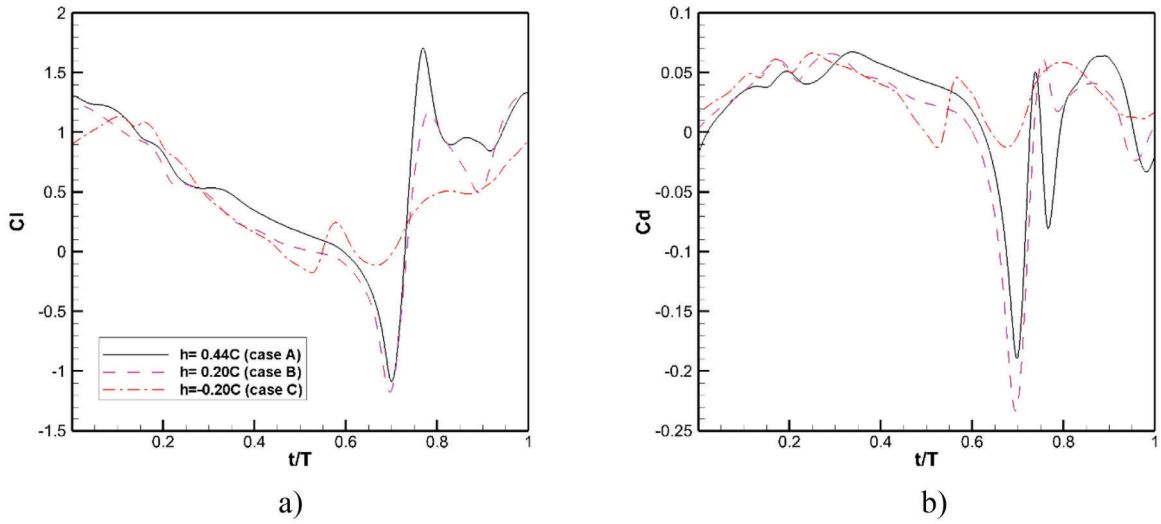

Fig. 16. Comparison of coefficients (a) lift and (b) drag for cases A–C on the hindfoil.

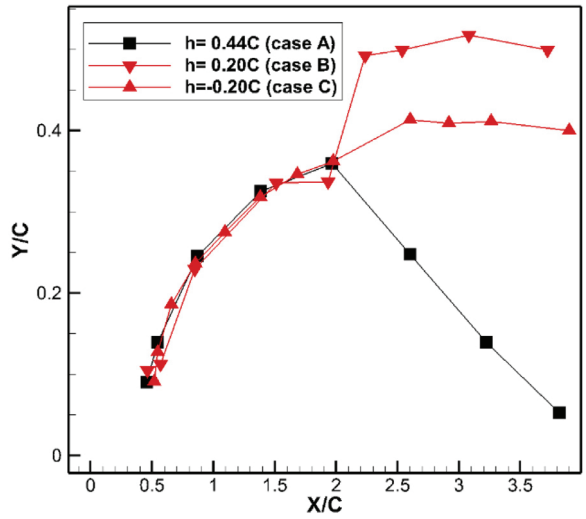

Fig. 17. Trajectory of LEV going around hindfoil for cases A–C.

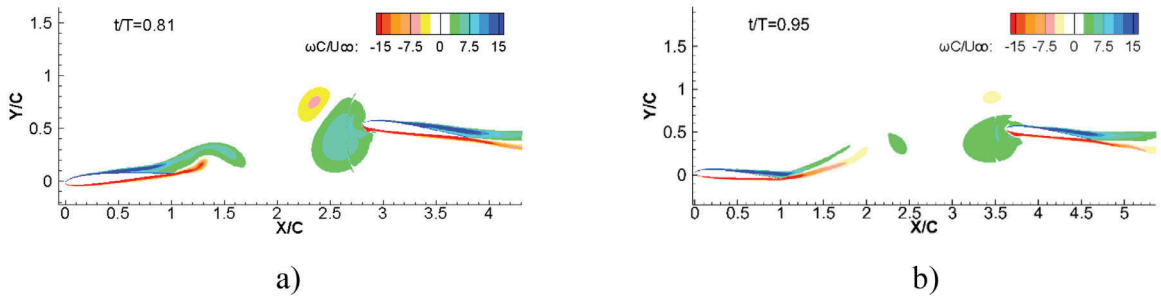

Fig. 18. Contours of non-dimensional vorticity for (a) case D, (b) case E.

reduced (Fig. 16(a)). Further lowering of hindfoil as in case C resulted in a complete change of events after the time $t/T = 0.7$ due to the fact that LEV did not collide with hindfoil. Similar trends can also be seen in drag force evolution in time as presented in Fig. 16 (b). The trajectories of LEV passing the vicinity of hindfoil for cases A–C are shown in Fig. 17. The trajectories are significantly different resulting in different force distribution over hindfoil. In cases A and B where LEV would split after colliding with hindfoil only the larger segment was tracked. For case A, the core of LEV (larger segment)

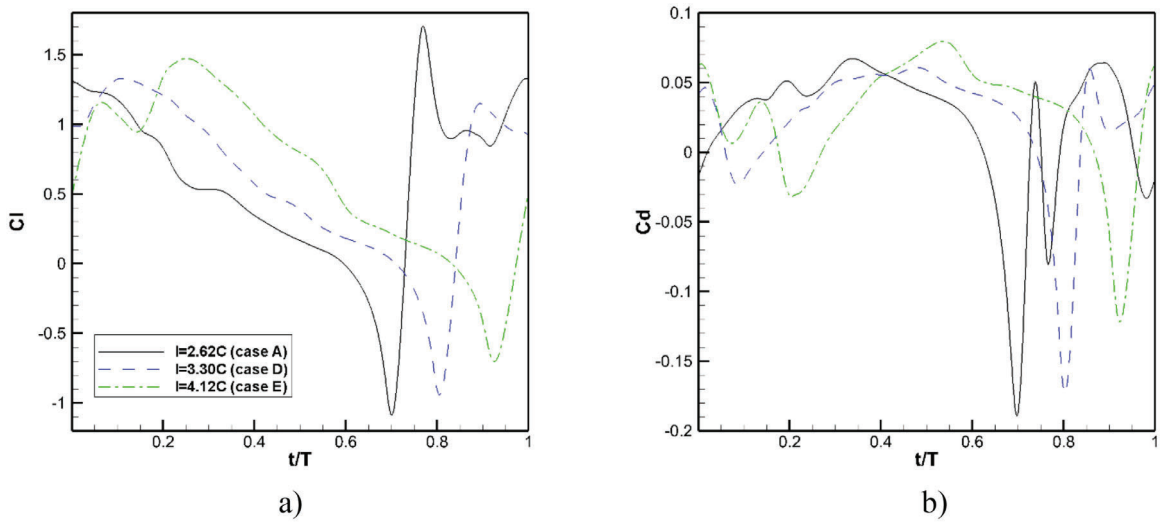

Fig. 19. Comparison of coefficients (a) lift and (b) drag for cases A, D, and E on the hindfoil.

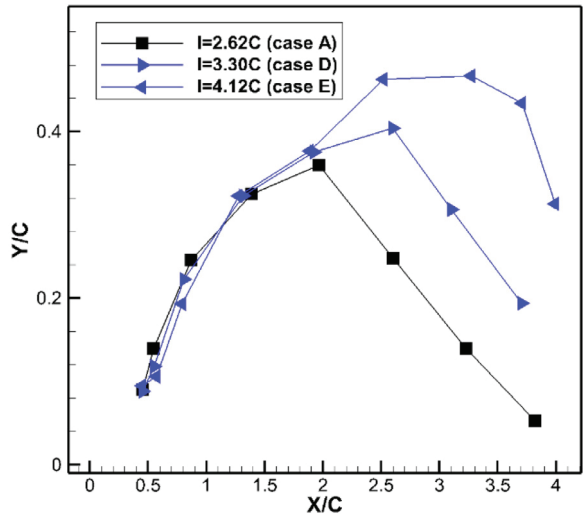

Fig. 20. Trajectory of LEV going around hindfoil for cases A, D, and E.

Table 6
Parameters and results for different horizontal spacings in Case 1.

Case	(l/C)	α_{hindfoil} (deg)	A (deg)	(h/C)	Cl_f	Cl_h	Cd_f	Cd_h	Cl_f+Cl_h	Cd_f+Cd_h	L/D_{tot}
case A	**2.62**	**7.216**	**14.1**	**0.440**	**1.0058**	**0.5850**	**0.2115**	**0.0210**	**1.5907**	**0.2325**	**6.84**
case D	3.30	7.216	14.1	0.440	1.0229	0.6056	0.2151	0.0226	1.6285	0.2377	6.85
case E	4.12	7.216	14.1	0.440	1.0360	0.6329	0.2167	0.0259	1.6689	0.2427	6.88

was pushed down below hindfoil and the opposite happened to the core of LEV in case B. For case C, there was no collision and LEV also passed over hindfoil.

6.1.3. Case 1: influence of horizontal spacing

The effect of horizontal spacing, l, on the trajectory of LEV was also investigated. All the parameters of Case 1 were kept unchanged but the horizontal spacing was allowed to change. The cases in this parametric study with their results are tabulated in Table 6.

The case A is the same as Case 1 with l/C = 2.62, and in cases B and C the horizontal spacings were increased to l/C = 3.30 and l/C = 4.12, respectively. The contours of vorticity for the time when LEV was in the vicinity of the hindfoil's leading edge are presented in Fig. 18. The contours in this figure should be compared with those of Fig. 12g of case A.

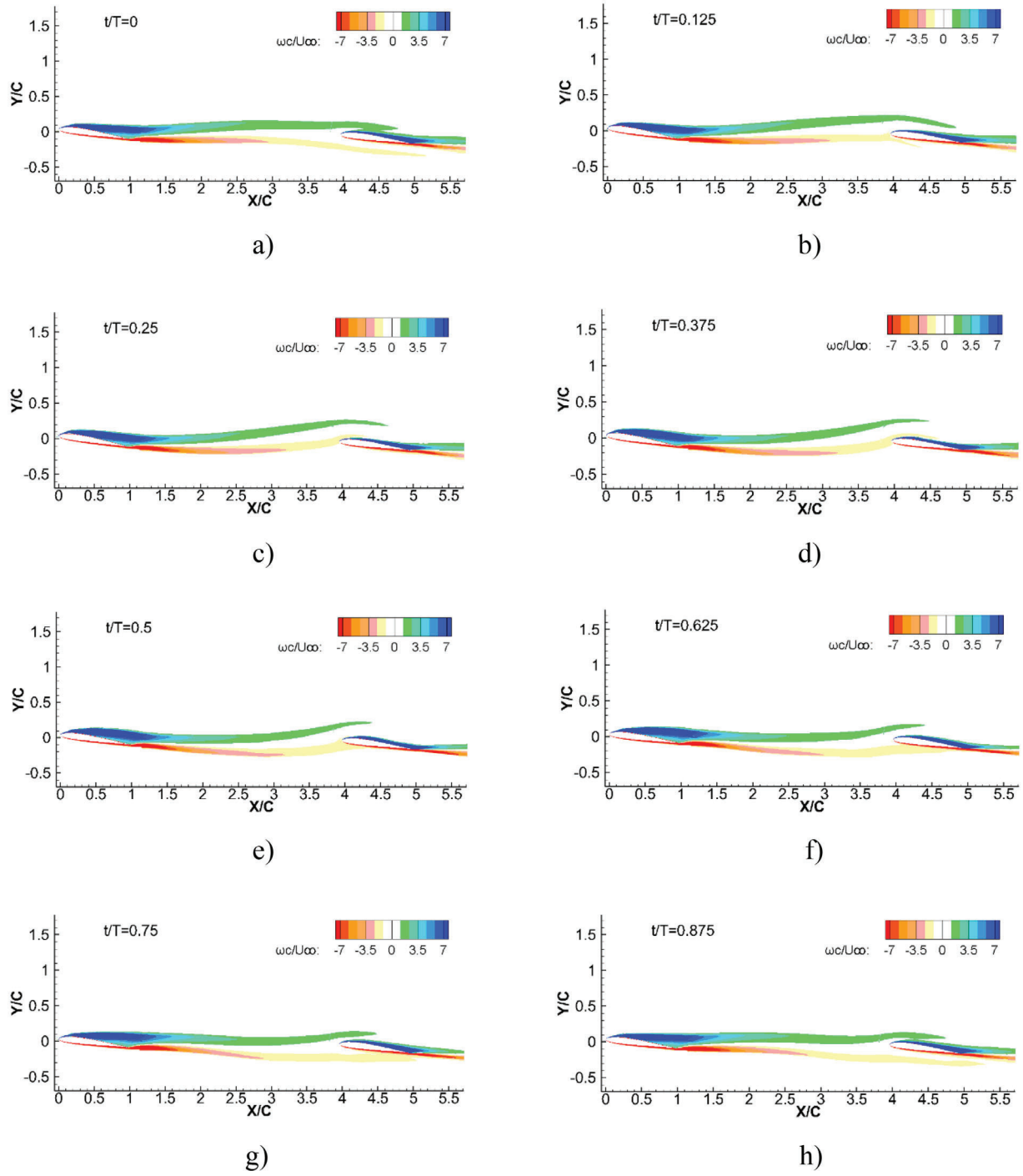

Fig. 21. Contours of non-dimensional vorticity for the optimum point of Case 2 at different times during one pitching time-cycle.

By moving hindfoil back, the time when LEV collided with hindfoil was delayed. At the time of collision, LEV was slightly weakened by the action of viscosity. The effect of this weakening can also be seen in the minimum values of lift and drag as presented in Fig. 19. During the interaction time, between $t/T = 0.7 - 0.75$ rapid switching from minimum to maximum values of lift were diminished and occurred at a later time. Similar trends can also be observed in the drag evolution in time. The altered trajectories of LEV due to this weakened interaction with hindfoil is presented in Fig. 20.

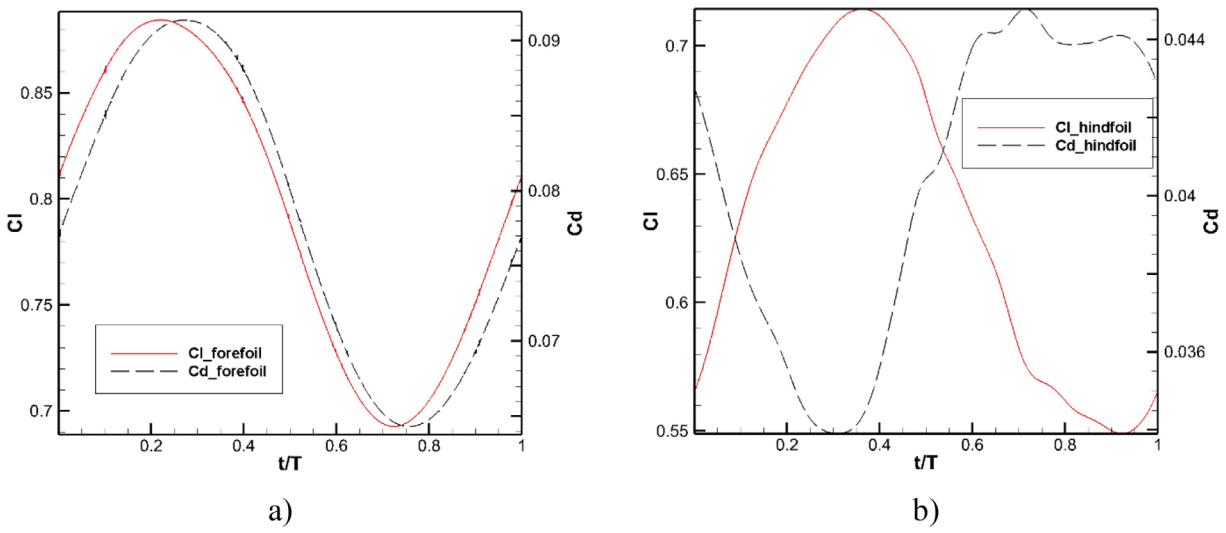

Fig. 22. Time-resolved lift and drag coefficient of (a) forefoil and (b) hindfoil (optimum point of Case 2).

Table 7
Properties of two airfoils in tandem: influence of vertical-spacing in Case 2.

Case	(l/C)	α_{hindfoil} (deg)	A (deg)	(h/C)	Cl_f	Cl_h	Cd_f	Cd_h	Cl_f+Cl_h	Cd_f+Cd_h	L/D_{tot}
case 2A	2.45	7.134	1	0.4	0.7838	0.7195	0.0787	0.065	1.50	0.14	10.44
case 2B	2.45	7.134	1	0.13	0.7892	0.6789	0.0783	0.053	1.47	0.13	11.21
case 2C	**4.45**	**7.134**	**1**	**-0.1345**	**0.7943**	**0.6305**	**0.0782**	**0.040**	**1.42**	**0.12**	**12.03**
case 2D	2.45	7.134	1	-0.4	0.7999	0.7055	0.0787	0.063	1.51	0.14	10.60

Table 8
Properties of two airfoils in tandem: influence of horizontal-spacing in Case 2.

Case	(l/C)	α_{hindfoil} (deg)	A (deg)	(h/C)	Cl_f	Cl_h	Cd_f	Cd_h	Cl_f+Cl_h	Cd_f+Cd_h	L/D_{tot}
case 2E	2.5	7.134	1	-0.1345	0.7799	0.5212	0.0826	0.0439	1.30	0.13	10.29
case 2F	3.5	7.134	1	-0.1345	0.7898	0.5869	0.0797	0.0424	1.38	0.12	11.27
case 2C	**4.45**	**7.134**	**1**	**-0.1345**	**0.7943**	**0.6305**	**0.0782**	**0.0403**	**1.42**	**0.12**	**12.03**

6.1.4. Case 2: pitching amplitude A = *1°*

In this case, we studied a low-amplitude oscillation for comparison with our previous case which had a relatively large amplitude. Here, a small pitching amplitude of $A = 1°$ about the same mean angle of attack of $a_0 = 8°$ (as in Case 1) was considered. Contours of vorticity for the optimum configuration at different times during one pitching time-cycle is presented in Fig. 21. The large vortex structures associated with dynamic stall of forefoil, LEVs and TEVs, were absent at these low-amplitude oscillations. However, interaction of the wakes from the top surface and bottom surface of forefoil with hindfoil was observed. Time evolution of lift and drag coefficients during one pitching time-cycle for both airfoils is presented in Fig. 22. Time variations for lift and drag of forefoil was very close to a single pitching airfoil and did not show any upstream influence from hindfoil. However, the changes in lift and drag in time for hindfoil was very different from a static airfoil. As shown in Fig. 22(b), coefficient of lift was below the static value of $C_l = 0.77$ and coefficient of drag was significantly below the static value of $C_d = 0.06$. This resulted in the superior aerodynamic performance (lift to drag ratio) for optimal configuration of Case 2 which had relatively low-amplitude oscillations in comparison to the optimal configuration of Case 1 with high-amplitude oscillations. However, the overall lift produced by optimal configuration of Case 1 was higher than the optimal configuration of Case 2 (see Table 4).

The results of a parametric study of geometric spacing changes between the two airfoils in Case 2 are presented below. The horizontal and vertical spacings between the two airfoils were changed around the optimum configuration separately. In each case one of the positioning parameters was changed and all the other parameters were kept fixed. All these cases for variation of vertical-spacing and horizontal-spacing study are tabulated in Table 7 and Table 8, respectively.

As shown in Table 7, by changing the vertical spacing between the two airfoils, drag of hindfoil was the most effected coefficient. By moving hindfoil upwards from the optimum configuration ($h/C = -0.1345$) to $h/C = 0.4$ as in cases 2C to 2A, drag and lift coefficient of hindfoil increased by 62% and 14%, respectively. Hence, it resulted in aerodynamic performance

Table 9
Comparison of aerodynamic coefficients of tandem configuration of Case 2 with the two airfoils placed separately in the flow.

	Cl	Cd	Cl_f+Cl_h	Cd_f+Cd_h	L/D_{tot}
Pitching forefoil in Case 2	0.794324	0.07818	1.425	0.118	12.03
Static hindfoil in Case 2	0.630464	0.040279			
Single pitching forefoil	0.806185	0.073238	1.577	0.133	
					11.83
Single static hindfoil	0.77103	0.060125			

being decreased by 13% from case 2C to 2A. However, lowering the hindfoil to $h/C = -0.4$ was also detrimental to performance by reducing it by 17%. This decrease in performance was due to the increases in interactions of forefoil's wake with hindfoil. Also as presented in Table 8, by increasing the horizontal spacing between the two airfoils from the $l/C = 2.5$ to $l/C = 4.45$ (maximum of our range) as in cases 2E to 2C, the aerodynamic performance increased from 10.29 to 12.03. Lift of hindfoil was the most effected coefficient. By increasing horizontal spacing as in case E to case C, hindfoil drag coefficient decreased by 9%, hindfoil lift increased by 17% and the total aerodynamic performance increased by 14.5%. This increase of performance has to be reversed eventually as the distance between the two airfoil is further increased. As shown in Table 9, aerodynamic performance of the two airfoils placed separately in the flow is less than the airfoils in optimum tandem configuration. Hence, as the horizontal spacing is increased to larger values we should lose any wake interaction influence.

7. Conclusions

In this study, the influence of having two specifically designed airfoils for low Reynolds number flows placed in a tandem configuration in comparison with acting as a single airfoil was considered. Two SD-7003 airfoils at low Reynolds number of 30,000 were used. The upstream airfoil (forefoil) oscillated with a pure-pitching motion at reduced frequency of $k = 0.5$ and a non-zero mean angle of attack of $a_0 = 8°$. The hindfoil was kept fixed with no movements. In an optimization study of the tandem geometry, the following design variables were allowed to change within a predetermined range: horizontal and vertical spacing between airfoils and angle of attack of hindfoil. Two separate optimizations to find the optimal tandem configuration were considered. The two cases were at two different order of magnitudes in pitching amplitudes of the upstream forefoil: Case 1 with $A = 14.1°$, where the forefoil went into deep stall and Case 2 with $A = 1°$ where the forefoil never stalled. For both optimum tandem configurations, the aerodynamic performance improved over having two well-separated airfoils.

In Case 1 (high-amplitude oscillations), multiple vortices (CW LEVs and CCW TEVs), as is characteristic of airfoils that go into deep stall, were produced over the top surface of forefoil during the pitching cycle. The most important criteria in the flow interaction was the formation of main LEV on the forefoil and the way it was convected downstream and collided with the leading edge of hindfoil. In the optimum configuration, at the moment of this collision there was a quick reversal in lift from minimum to maximum value in a very short period of time $t/T = 0.7 - 0.75$. Due to this collision, the main LEV was broken into two pieces and the core (larger piece) went just under the hindfoil and the smaller piece went over the top surface of hindfoil. The perfect timing and positioning of how LEV collided with hindfoil and the nature of its breakup into two pieces resulted in the maximum performance for the optimum tandem configuration. The aerodynamic performance for the optimum tandem configuration went from 6.42 for the sum of two well-separated airfoils to 6.84, an improvement of 6.5%.

In Case 2 (low-amplitude oscillations), forefoil never stalled during the pitching cycle. However, the flow over hindfoil was influenced by the wake of forefoil being convected towards it. As in Case 1, this case also improved the aerodynamic performance from 11.83 for the sum of two well-separated airfoils to 12.03 for the tandem configuration. This case produced lower overall lift force in comparison to Case 1. However, there was a significant improvement in total performance implying that it would be more suitable for long duration.

Appendix A

The boundary conditions used in the turbulence model of Menter et al. [15,16] are presented in Table A.1.

Table A.1
Boundary conditions used on turbulence model of [15,16].

	Velocity (m/s)	Pressure(pascal)	$k(m^2/s^2)$	$\omega(1/s)$	γ	$Re_{\theta t}$
Inlet	[3.77 , 0]	$\partial p/\partial n = 0$	8.53e-05	0.44	1	1061.11
Outlet	$\partial U/\partial n = 0$	$P = 0$ (Ambient conditions)	$\partial k/\partial n = 0$	$\partial\omega/\partial n = 0$	$\partial\gamma/\partial n = 0$	$\partial Re_{\theta t}/\partial n = 0$
Walls	[0,0]	$\partial p/\partial n = 0$	~ 0	$\sim 10^8$	$\partial\gamma/\partial n = 0$	$\partial Re_{\theta t}/\partial n = 0$

References

[1] G.Q. Zhang, S.C.M. Yu, Unsteady aerodynamics of a morphing tandem-wing unmanned aerial vehicle, J. Aircr. 49 (2012) 1315–1323, doi:10.2514/1.C031652.
[2] M. Hassanalian, A. Abdelkefi, Classifications, applications, and design challenges of drones: a review, Prog. Aerosp. Sci. 91 (2017) 99–131, doi:10.1016/j.paerosci.2017.04.003.
[3] M.L. Mantia, P. Dabnichki, Effect of the wing shape on the thrust of flapping wing, Appl. Math. Model. 35 (2011) 4979–4990, doi:10.1016/j.apm.2011.04.003.
[4] D.J. Kamari, M. Tadjfar, A. Madadi, Optimization of SD7003 airfoil aerodynamic performance using TBL and CBL at low Reynolds numbers, Aerosp. Sci. Technol. 79 (2018) 199–211, doi:10.1016/j.ast.2018.05.049.
[5] M. Tadjfar, D.J. Kamari, Optimization of flow control parameters over SD7003 airfoil with synthetic jet actuator, J. Fluids Eng. 142 (2020), doi:10.1115/1.4044985.
[6] N.M. Tousi, M. Coma, J.M. Bergada, J. Pons-Prats, F. Mellibovsky, G. Bugeda, Active flow control optimization on SD7003 airfoil at pre and post-stall angles of attack using synthetic jets, Appl. Math. Model. 98 (2021) 435–464, doi:10.1016/j.apm.2021.05.016.
[7] D.F. Scharpf, T.J. Mueller, Experimental study of a low Reynolds number tandem airfoil configuration, J. Aircr. 29 (1992) 231–236, doi:10.2514/3.46149.
[8] R. Jones, D.J. Cleaver, I. Gursul, Aerodynamics of biplane and tandem wings at low Reynolds numbers, Exp. Fluids 56 (2015) 1–25, doi:10.1007/s00348-015-1998-3.
[9] T. Faure, L. Hetru, O. Montagnier, Aerodynamic features of a two-airfoil arrangement, Exp. Fluids 58 (2017), doi:10.1007/s00348-017-2429-4.
[10] T. Faure, L. Dumas, O. Montagnier, Numerical study of two-airfoil arrangements by a discrete vortex method, Theor. Comput. Fluid Dyn. 34 (2020) 79–103, doi:10.1007/s00162-019-00511-0.
[11] D. Rival, R. Manejev, C. Tropea, Measurement of parallel blade-vortex interaction at low Reynolds numbers, Exp. Fluids 49 (2010) 89–99, doi:10.1007/s00348-009-0796-1.
[12] T. Lee, Flow past two in-tandem airfoils undergoing sinusoidal oscillation, Exp. Fluids 51 (2011) 1605–1621, doi:10.1007/s00348-011-1173-4.
[13] K.B. Lua, H. Lu, X.H. Zhang, T.T. Lim, K.S. Yeo, Aerodynamics of two-dimensional flapping wings in tandem configuration, Phys. Fluids 28 (2016), doi:10.1063/1.4971859.
[14] K. Balla, R. Sevilla, O. Hassan, K. Morgan, An application of neural networks to the prediction of aerodynamic coefficients of aerofoils and wings, Appl. Math. Model. 96 (2021) 456–479, doi:10.1016/j.apm.2021.03.019.
[15] F.R. Menter, R.B. Langtry, S.R. Likki, Y.B. Suzen, P.G. Huang, S. Volker, A correlation-based transition model using local variables-part I: model formulation, J. Turbomach. 128 (2006) 413–422, doi:10.1115/1.2184352.
[16] F.R. Menter, R.B. Langtry, S. Volker, Correlation-based transition modeling for unstructured parallelized computational fluid dynamics codes, AIAA J. 47 (2009) 2894–2906, doi:10.2514/1.42362.
[17] M. Tadjfar, E. Asgari, Active flow control of dynamic stall by time-averaged of continuous jet flow at Reynolds number of 1 $\times$ 106, J. Fluids Eng. 140 (2018), doi:10.1115/1.4037841.
[18] M. Tadjfar, E. Asgari, The role of frequency and phase difference between the flow and the actuation signal of a tangential synthetic jet on dynamic stall flow control, J. Fluids Eng. 140 (2018), doi:10.1115/1.4040795.
[19] M.V. Ol, L. Bernal, C.K. Kang, W. Shyy, Shallow and deep dynamic stall for flapping low Reynolds number airfoils, Exp. Fluids 46 (2009) 883–901, doi:10.1007/s00348-009-0660-3.
[20] D. Rival, C. Tropea, Characteristic of pitching and plunging airfoils under dynamic-stall conditions, J. Aircr. 47 (2010) 80–86, doi:10.2514/1.42528.